MULTIFOCAL INTERFEROMETRIC SYNTHETIC APERTURE MICROSCOPY

BY

YANG XU

THESIS

Submitted in partial fulfillment of the requirements
for the degree of Master of Science in Electrical and Computer Engineering
in the Graduate College of the
University of Illinois at Urbana-Champaign, 2014

Urbana, Illinois

Adviser:

Associate Professor P. Scott Carney

ABSTRACT

We extend interferometric synthetic aperture microscopy (ISAM) to optical coherence tomography (OCT) data collected with multiple positions of the focal plane. Multifocal ISAM achieves spatially invariant resolution like ISAM by applying the solution of the inverse problem to the forward model for each channel. A general regularized solution eliminates artifacts that affect multibeam OCT while achieving better signal-to-noise ratio over the entire image than is possible with single-focus ISAM. We present detailed theory, computer simulation, experimental results and analysis.

To my parents and Yuyan, for their love and support.

ACKNOWLEDGMENTS

This research was supported in part by a grant from the National Institutes of Health (NIBIB, R01 EB012479).

TABLE OF CONTENTS

LIST OF FIGURES

CHAPTER 1

INTRODUCTION

1.1 Working Principles of OCT

Optical coherence tomography (OCT), is an optical imaging method that is able to reveal the 3D structure of optical scattering media with micron-resolution [1, 2, 3, 4, 5, 6, 7]. OCT has proved useful in many fields including ophthalmology [8, 9, 10, 11, 7, 12, 13], dermatology [14, 15, 16], and cardiology [17]. In addition, more novel applications [18, 19] are being developed by researchers all over the world.

The working principle of OCT is similar to that of ultrasound, in that both try to measure the distributed back-scattering of the incident wave to reconstruct the distributed scattering coefficient at each position of the sample.

There are many variants of OCT, namely time domain OCT (TD-OCT) [20], spectral domain OCT (SD-OCT) [21, 20, 22], and swept source OCT [23]. Each has a slightly different physical configuration, but they all produce equivalent data under appropriate transformations. There are also various geometries, such as wide-field [24], rotational [25] and scanning geometries [26]. Here we take focused scanning spectral domain OCT as an example. The setup for SD-OCT includes a broadband source connected to a fiber-based Michelson interferometer, where one of its arms is a fixed mirror, and on the other arm is a focusing lens projecting the beam into the sample. The beam illuminates the sample, and is partially scattered back and again collected by the focusing lens. The collected light interferes with the light from the other arm and is recorded by a spectrometer.

A-scan, B-scan, and C-scan are the terms from ultrasonography used to describe the dimensionality of the scan, which also apply to OCT. When the scanning beam is focused at some transverse position (x, y) of the sample,

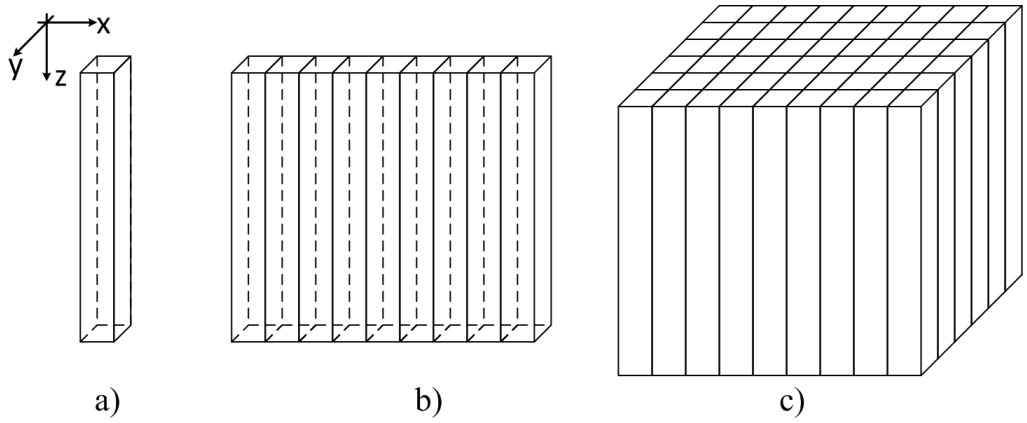

Figure 1.1: Illustration of a) A-scan, b) B-scan, and c) C-scan.

an A-scan can be performed to detect the one-dimensional structure of the sample along z-direction, as is shown in Figure 1.1 a). Multiple A-scans along a certain axis form a B-scan, from which the cross sectional structure of the sample can be obtained, as is shown in Figure 1.1 b). Similarly, a series of B-scans along the other dimension form a C-scan, which is a volume scan of the sample, as is shown in Figure 1.1 c).

By performing a C-scan over an area of a sample, the sample structure can be reconstructed using a Fourier transform of the collected dataset. This relation is based on two assumptions, the first Born approximation and pencil-beam approximation. The first Born approximation assumes single-scattering and neglects higher-order scattering, which has proved to be a good approximation for many applications including biological tissue imaging [26]. Nevertheless, multiple-scattering artifacts have been observed in some situations [27, 28]. The pencil-beam approximation assumes that the width of the focused, scanning beam remains constant along depth direction, which is, in general, a bad approximation. The variation of the focused Gaussian beam width along the propagation direction depends on the numerical aperture (NA) of the system. Figure 1.2 shows the focused Gaussian beam $1/e^2$ intensity contour of 1μm wavelength light with various NA. It can be observed from the figure that the pencil-beam approximation can only be applied to low-NA system (≤ 0.2). However, for high-NA systems, crucial for achieving high transverse resolution, this assumption is no longer valid, as the beam width diverges quickly far away from the focusing plane. This causes the decay in transverse resolution of OCT reconstructions at positions

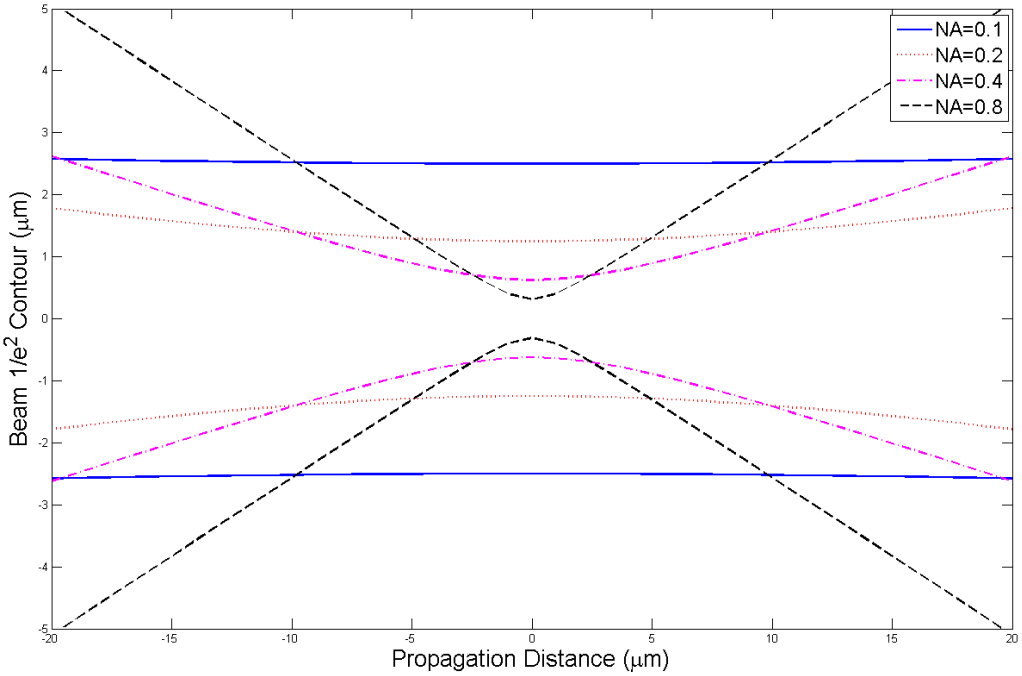

Figure 1.2: Beam $1/e^2$ contour of focused Gaussian beam at 1μm wavelength with various NA.

far from the focusing plane.

1.2 Trade-off in OCT between Resolution and Imaging Depth

In OCT, there are two important figures of merit, imaging depth and transverse resolution. However, by the laws of physics, it is theoretically impossible to improve both at the same time. For a given OCT system, the transverse resolution at certain depth is equivalent to the width of the scanning beam at that depth. The transverse resolution is best on the focal plane, where the scanning beam has minimum beam width. The beam-waist width is

$$w_0 = \frac{\lambda}{2n \cdot \mathbf{NA}}. \tag{1.1}$$

The transverse resolution degrades as the position of reconstruction is further away from focal plane, where the scanning beam diverges in width,

$$w(z) = \sqrt{w_0^2 + \left[\frac{\lambda(z - z_0)}{\pi n w_0}\right]^2}. \tag{1.2}$$

Because of the decay in transverse resolution, the reconstructed image becomes defocused at positions far away from the focal plane. Therefore, the usable imaging depth of the OCT system is usually taken to be within a Rayleigh range (Z_R) of the focal plane. The Rayleigh range is defined as the distance from the focal plane to the plane where $w(z) = \sqrt{2}w_0$. Here we take the imaging depth to be the confocal range which is twice the Rayleigh range so that the worst transverse resolution is $\sqrt{2}w_0$. The confocal range of an OCT system can be expressed as

$$\textbf{Confocal Range} = 2Z_R = 2n\pi w_0^2/\lambda, \tag{1.3}$$

which is proportional to transverse resolution square.

In Figure 1.3, the curve represents all combinations of imaging depth and transverse resolution theoretically possible at wavelength of 1μm and with refractive index of 1.4. For example, if the desired transverse resolution is 1.2μm on the above mentioned condition, which can be achieved by using a 0.3 NA focusing lens, the achievable imaging depth is 12.7μm, as can be seen at the lower sample point. On the other hand, if the imaging depth is increased to 112μm, which can be implemented using a 0.1 NA focusing lens, the best possible transverse resolution degrades to 3.6μm, as can be seen at the upper sample point.

Although OCT is limited by the above-mentioned trade-off, it is possible to mitigate the trade-off by improving either the physical setup or the reconstruction algorithm. There are two existing solutions, interferometric synthetic aperture microscopy (ISAM) and multifocal OCT, each having its own advantages and challenges.

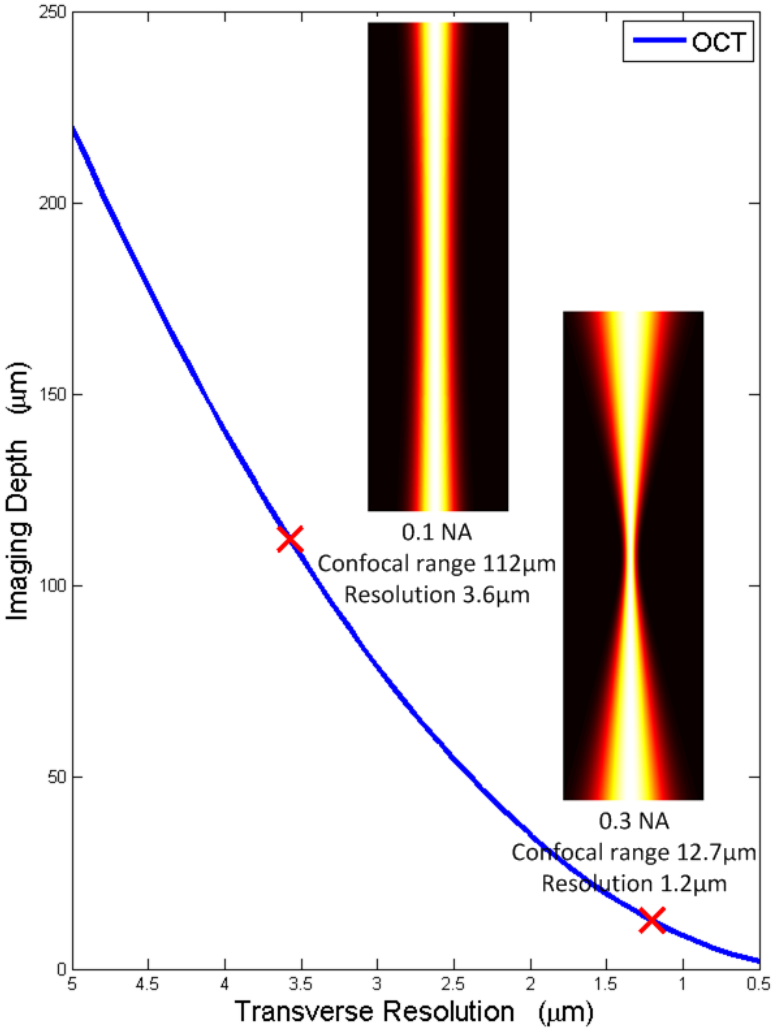

Figure 1.3: Trade-off between imaging depth and transverse resolution in OCT.

1.3 Multifocal OCT

Multifocal OCT, also called multibeam OCT or multichannel OCT [29, 30], is a parallel version of OCT, where multiple apertures are used simultaneously in scanning, as is shown in Figure 1.4. Each aperture is focused at a different depth of the sample during the scan. One set of data is collected from each aperture.

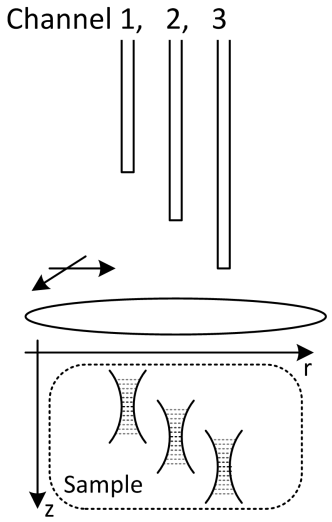

Figure 1.4: Physical setup of multifocal OCT.

In multifocal OCT, since there are multiple apertures scanning simultaneously, each aperture receives not only the back-scattered light contributed by its own illumination, but also the back-scattering from the illumination of other apertures, as is seen in Figure 1.5. If the illumination of each aperture is coherent to some degree, i.e. if they share the same light source and the difference in optical path-length is less than the coherent length of the light source, the aperture crosstalk will be detected by the interferometer. This will result in multiple ghost images overlapping each other in the reconstruction. For example, if we assume three apertures are scanning simultaneously and the waist planes of the Gaussian beams are coherent with each other, the reconstruction from aperture 1 is shown in Figure 1.6. This effect is in general undesirable, and can be eliminated either by using a different light source for each aperture (which is expensive), or inserting a fiber bundle before each aperture so that the optical path-length is much larger than the source coherent length.

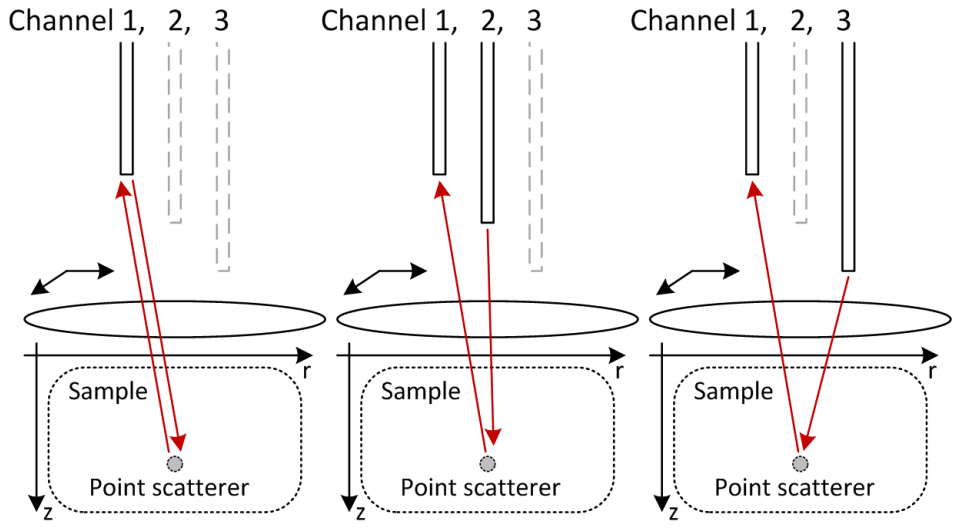

Figure 1.5: Illustration of the different components of the aperture crosstalk in multifocal OCT.

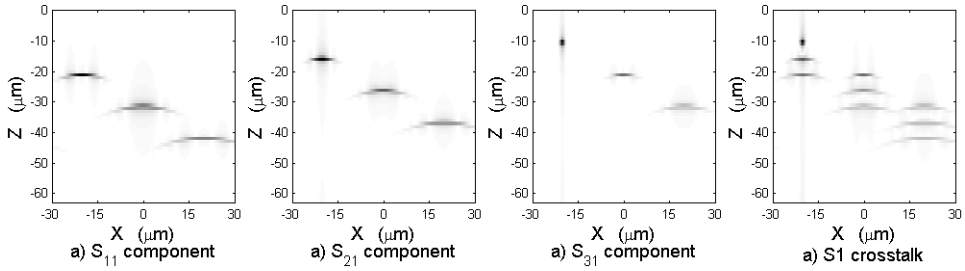

Figure 1.6: Panels a), b), and c) are simulated components of multifocal OCT signal of aperture 1 contributed by a) aperture 1, b) aperture 2, and c) aperture 3. Panel d) is the overall OCT signal of aperture 1.

An image stitching method is used to combine each set of data. A simulation of cross-sectional scan (B-scan) in 2D with noise included is done to illustrate the method. The sample used in the simulation consists of a series of point scatters positioned along the diagonal axis. The horizontal axis corresponds to the transverse direction, while the vertical axis represents the depth into the sample. Three apertures focused at -20 μm, -60 μm and -100 μm are used in the simulation, which are shown in Figure 1.7 a), b) and c) respectively. As is illustrated in Figure 1.7 d), the image stitching method takes the part with the best transverse resolution from each set of data, and stitches them into the final reconstruction. Compared with each set of OCT data, the multifocal OCT image shows an improved resolution over the whole depth, or from another point of view, enables a larger imaging depth.

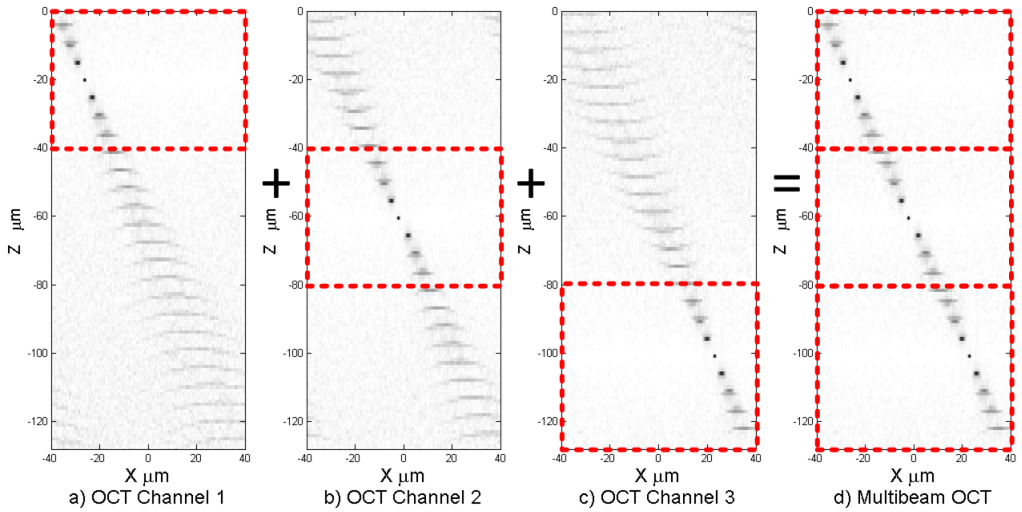

Figure 1.7: Illustration of the image stitching method.

Consider the case of a multifocal OCT system with 3 identical apertures. The distance between two adjacent focal planes is set to be 1 confocal range, (i.e. three apertures focusing at the depth of 0.5, 1.5 and 2.5 confocal ranges). In this case, the transverse resolution in reconstruction is always equal to or better than $\sqrt{2}w_0$, which is similar to our assumption in OCT. Figure 1.8 plots the trade-off curve of multifocal OCT compared with OCT. As three stacked apertures are used, for any value of transverse resolution, multifocal OCT provides 3 times the imaging depth compared with OCT; or on the other hand, for the same desired imaging depth, multifocal OCT can achieve improved transverse resolution compared to OCT.

Multifocal OCT also faces challenges such as intensity discontinuities along stitching edge in the reconstructed image [29, 30]. Although artificial blending can be used to mitigate this effect [31], it is not physically derived and thus does not always provide accurate image reconstruction.

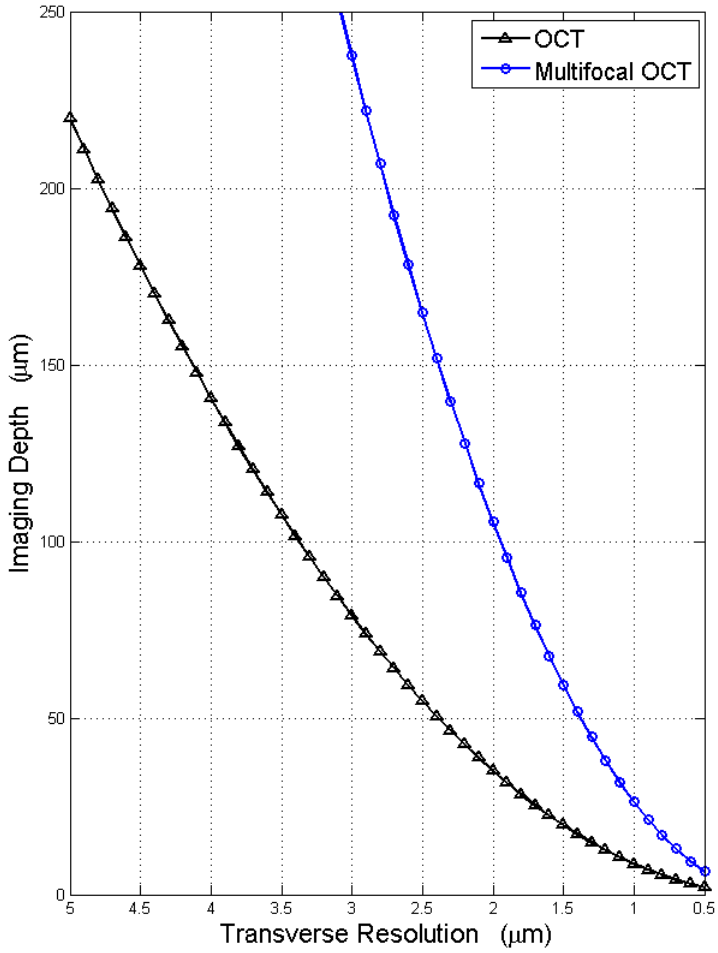

Figure 1.8: The trade-off curve of multifocal OCT compared with OCT.

1.4 Interferometric Synthetic Aperture Microscopy

The ISAM experiment is similar to that of OCT. ISAM takes the OCT data and corrects for the spreading of the beam using the solution to the inverse problem of OCT [32, 33, 34]. The algorithm can be efficiently implemented using a frequency domain resampling technique [33, 26], which can be expressed by Equation (1.4) [26], where $|S\rangle$ represents the OCT data.

$$\begin{aligned}\langle \mathbf{r}|\eta\rangle = w(z-z_0)\int \mathrm{d}^2 k_\parallel \left\langle \mathbf{r}_\parallel|\mathbf{k}_\parallel\right\rangle \int \mathrm{d}\beta \left\langle z|-\beta\right\rangle \\ \times H_F^{-1}\left\langle \mathbf{k}_\parallel, \frac{1}{2}\sqrt{\beta^2+\mathbf{k}_\parallel^2}, z_{0n}|S\right\rangle \end{aligned} \tag{1.4}$$

Because the depth of focus of OCT is infinitely extended by applying the algorithm, ISAM is able to provide spatially invariant resolution, as opposed to the decaying resolution of OCT along depth axis. ISAM has been validated and is proved to provide accurate reconstruction with good resolution [32, 35].

However, ISAM faces the challenge of signal-to-noise ratio (SNR) decreasing with 1/z, which limits its effective imaging depth [32]. Assume SNR at focus is $\mathbf{SNR_0}$ (linear), and the smallest tolerable SNR is $\mathbf{SNR_L}$, imaging depth is limited by

$$\frac{\mathbf{SNR_0}}{\omega(z)/\omega_0} \geq \mathbf{SNR_L}, \tag{1.5}$$

which has the following solution:

$$\mathbf{SNR\ Range} = \frac{2\pi n\omega_0^2}{\lambda_0}\sqrt{\left(\frac{\mathbf{SNR_0}}{\mathbf{SNR_L}}\right)^2 - 1}. \tag{1.6}$$

Figure 1.9 plots the trade-off curve of ISAM when $\mathbf{SNR_0/SNR_L = 10}$. Compared with multifocal OCT, ISAM further shifts the curve to the upright direction, mitigating the trade-off. This can be partially explained by the fact that human eye is less sensitive to decaying SNR than decaying resolution.

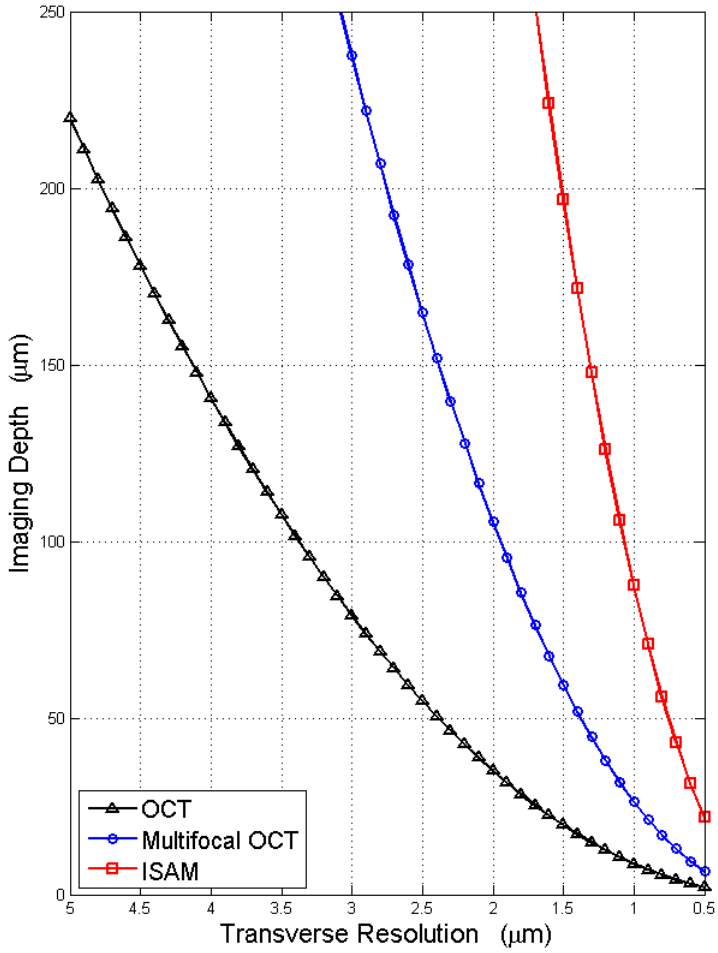

Figure 1.9: The trade-off curve of multifocal OCT compared with OCT.

CHAPTER 2

METHODOLOGY

In this chapter, some notation and methodology useful in subsequent chapters are introduced.

2.1 Notation

Following [26], all equations in this thesis are written in Dirac (bra-ket) notation and use similar symbol conventions. In this section, some basic symbol conventions will be introduced to aid the understanding of the equations appearing in this thesis.

The symbols used in this thesis include $\mathbf{r}$, $\mathbf{k}$, $\mathbf{r}_\parallel$, $\mathbf{k}_\parallel$, z, and k_z. The symbols $\mathbf{r}$ and $\mathbf{k}$ are vectors in $\mathbb{R}^3$, which describe the position in three-dimensional spatial and frequency domain, respectively, as are shown in Equation (2.1) and (2.2). In this thesis, z is defined as the direction of propagation of the beam; and x and y directions are defined as the parallel directions. Therefore, $\mathbf{r}_\parallel$ and $\mathbf{k}_\parallel$ are vectors in $\mathbb{R}^2$, which describes the position in two-dimensional spatial and frequency domain respectively, as shown in Equations (2.3) and (2.4). Directions z and k_z are in $\mathbb{R}^1$ and describe the position in the z-axis in spatial and frequency domain; that is,

$$\mathbf{r} = \begin{pmatrix} x \\ y \\ z \end{pmatrix}, \tag{2.1}$$

$$\mathbf{k} = \begin{pmatrix} k_x \\ k_y \\ k_z \end{pmatrix}, \tag{2.2}$$

$$\mathbf{r}_{\parallel} = \begin{pmatrix} x \\ y \end{pmatrix}, \tag{2.3}$$

$$\mathbf{k}_{\parallel} = \begin{pmatrix} k_x \\ k_y \end{pmatrix}. \tag{2.4}$$

The vector $|\mathbf{r}\rangle$ will represent a basis vector, labeled by $\mathbf{r}$ for $L_2(\mathbb{R}^3)$, the space of square-integrable functions on $\mathbb{R}^3$. We will also use another set of basis vectors $|\mathbf{k}\rangle$ with the relationship to $|\mathbf{r}\rangle$ that $\langle \mathbf{r}|\mathbf{k}\rangle = (2\pi)^{-3/2} e^{i\mathbf{k}\cdot\mathbf{r}}$. It will be useful to recognize that $|\mathbf{r}\rangle = |x\rangle\,|y\rangle\,|z\rangle$; that is, $|\mathbf{r}\rangle$ may be written as a vector product of basis vectors in $L_2(\mathbb{R})$. Thus we will construct mixed basis vectors $\left|\mathbf{k}_{\parallel}, z\right\rangle = \left|\mathbf{k}_{\parallel}\right\rangle |z\rangle$ such that $\langle \mathbf{r}'|k_x, k_y, z\rangle = (2\pi)^{-1} e^{ik_x x' + ik_y y'} \delta(z' - z)$, etc.

The symbol $|\eta\rangle$ represents susceptibility, or the ability of the material to scatter light. It is a vector in $L_2(\mathbb{R}^3)$. $\langle \mathbf{r}|\eta\rangle$ is the representation of the susceptibility in three-dimensional spatial domain. Similarly, $\langle \mathbf{k}|\eta\rangle$ represents three-dimensional susceptibility distribution of the sample in frequency domain, which relates to $\langle \mathbf{r}|\eta\rangle$ through a three-dimensional Fourier transform. Since the Fourier transform can be performed on a single dimension in a multidimensional matrix, without affecting the basis of other dimensions, kets like $|S\rangle \in L_2(\mathbb{R}^4)$ can also be projected onto the spatial domain coordinates on some dimensions and onto frequency domain coordinates on other dimensions, which is represented in a way such as $\left\langle \mathbf{k}_{\parallel}, k, z_{0n}|S\right\rangle$.

2.2 Pseudo-inverse

Operators represent the linear mapping from one vector space to another. The general form of an operator is

$$P = \sum_{k,k'} |k'\rangle\, P_{kk'}\, \langle k|\,, \tag{2.5}$$

where $P_{kk'}$ represents matrix elements in the matrix P. The operator takes a vector $|v\rangle$ and map to a vector $|s\rangle$, which is denoted as

$$|s\rangle = P\,|v\rangle = \sum_{k,k'} |k'\rangle\, P_{kk'}\, \langle k|v\rangle\,. \tag{2.6}$$

By finding proper bases in both vector spaces, operator P can be written as the transformation represented by a quasi-diagonal matrix,

$$P = \sum_j |j_2\rangle \, \sigma_j \, \langle j_1| \,, \tag{2.7}$$

where $j = 1, 2, 3...$ labels each basis. This representation is called the singular value decomposition of operator P, with singular values σ_j, and singular vectors $|j_2\rangle$ and $\langle j_1|$. The common way to find a set of such basis is to solve for the eigenvector $|j_1\rangle$ in the eigenvalue problem

$$P^* P \, |j_1\rangle = \sigma_j^2 \, |j_1\rangle \,, \tag{2.8}$$

and use

$$|j_2\rangle = \sigma_j^{-1} P \, |j_1\rangle \tag{2.9}$$

to find the vector $|j_2\rangle$ corresponding to each $|j_1\rangle$ for all j for which $\sigma_j \neq 0$.

If all the σ_j are nonzero, the inverse operator of P can be expressed as

$$P^{-1} = \sum_j |j_1\rangle \, \sigma_j^{-1} \, \langle j_2| \,. \tag{2.10}$$

However this condition is not always met in reality. For operators with some $\sigma_j = 0$, only the least-squared-error inverse operator

$$P^+ = \sum_{\sigma_j \neq 0} |j_1\rangle \, \sigma_j^{-1} \, \langle j_2| \tag{2.11}$$

can be calculated. P^+ is called the pseudoinverse of P. Another useful way to calculate P^+ is

$$P^+ = (P^* P)^{-1} P^*, \tag{2.12}$$

which is used in later sections.

2.3 Regularization

The pseudoinverse gives the least-squared-error result in theory, when the dataset it acts on is ideal. In reality, the dataset always contains noise and pseudoinverse can sometimes be very sensitive to noise. For example,

consider the case

$$|W\rangle = P^{+}\,|S_{noisy}\rangle = \sum_{\sigma_j \neq 0} |j_1\rangle\, \sigma_j^{-1}\, \langle j_2|S_{noisy}\rangle\,, \tag{2.13}$$

where

$$|S_{noisy}\rangle = |Signal\rangle + |Noise\rangle\,. \tag{2.14}$$

When there is a particular σ_j which is very small, the corresponding σ_j^{-1} in the $|j_1\rangle\, \sigma_j^{-1}\, \langle j_2|S_{noisy}\rangle$ component of the pseudoinverse is very large. This greatly amplifies the noise component $\langle j_2|S_{noisy}\rangle$, which contaminates the result $|W\rangle$.

To mitigate the effect, regularization can be applied. The regularized pseudoinverse can be derived by replacing the σ_j^{-1} by the function $R[\sigma_j^{-1}]$, so that

$$P^{+} = \sum_{j} |j_1\rangle\, R[\sigma_j^{-1}]\, \langle j_2|\,. \tag{2.15}$$

Depending on various noise models, the function $R[\sigma_j^{-1}]$ can take various forms. For example, when the noise is zero-mean and multiplicative, Tikhonov regularization, which has the form

$$P^{+} = \sum_{j} |j_1\rangle\, \frac{\sigma_j}{\sigma_j^2 + \lambda}\, \langle j_2|\,, \tag{2.16}$$

provides optimum results. For zero-mean and multiplicative noise, $\lambda = N^2$ is the optimum parameter to achieve least square error solution.

2.4 Method of Stationary Phase

The method of stationary phase provides a convenient way of computing the integration of functions which are modulated by a rapidly evolving phase, where there exists a point near which the evolution of phase stops. This method is used in the derivation in the later sections. In this section, we will briefly illustrate the one-dimensional case of the method of stationary phase.

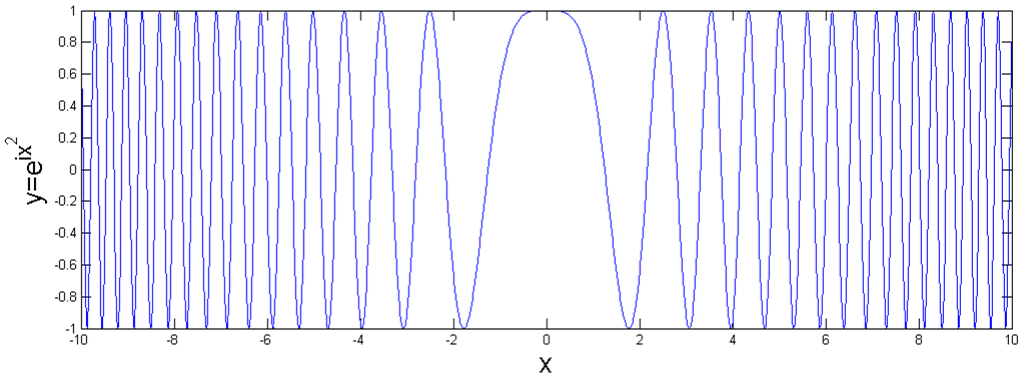

Figure 2.1: Plot of the real part of a function with a stationary point at $x = 0$.

This above-mentioned integration can be typically represented by

$$\int_{-\infty}^{\infty} f(x)e^{i\phi(x)}\mathrm{d}x, \tag{2.17}$$

where $f(x)$ represents an slowly varying envelop, and $\phi(x)$ describes the evolution of phase along the axis of integration.

To find if there exists a point near which $\phi(x)$ stops to evolve, we take

$$\frac{d}{\mathrm{d}x}\phi(x) = 0. \tag{2.18}$$

If a solution exists, the corresponding point is called a stationary point. Here we label it x_0. An example of such point is shown in Figure 2.1.

We then take a Taylor series expansion of $\phi(x)$, and keep the first three terms. Note since the first derivative, $\phi'(x_0) = 0$, only two terms are left.

$$\phi(x) = \phi(x_0) + \cancelto{0}{\phi'(x_0)(x - x_0)} + \frac{1}{2}\phi''(x_0)(x - x_0)^2 + ... \tag{2.19}$$

We substitute the Taylor series expansion of $\phi(x)$ from Equation (2.19) into Equation (2.17). As can be seen in Figure 2.1, the contribution to the integral mainly comes from the stationary point. Thus, we can plug in $x = x_0$

in to $f(x)$ and get

$$\begin{aligned}
&\int_{-\infty}^{\infty} f(x)e^{i\phi(x)}\mathrm{d}x \\
\approx\ &\int_{-\infty}^{\infty} f(x)\exp\left[i\phi(x_0)+\frac{i}{2}\phi''(x_0)(x-x_0)^2\right]\mathrm{d}x \\
\approx\ &f(x_0)e^{i\phi(x_0)}\int_{-\infty}^{\infty}\exp\left[\frac{i}{2}\phi''(x_0)(x-x_0)^2\right]\mathrm{d}x. \qquad (2.20)
\end{aligned}$$

The remaining integration in Equation (2.20) can be evaluated using a close loop integration in the complex plane to get the closed form solution, that is

$$\int_{-\infty}^{\infty}\exp\left[\frac{i}{2}\phi''(x_0)(x-x_0)^2\right]\mathrm{d}x=\sqrt{\frac{2\pi}{\phi''(x_0)}}e^{i\pi/4}. \qquad (2.21)$$

Thus the integration has the following result:

$$\int_{-\infty}^{\infty} f(x)e^{i\phi(x)}\mathrm{d}x\approx f(x_0)e^{i\phi(x_0)}\sqrt{\frac{2\pi}{\phi''(x_0)}}e^{i\pi/4}. \qquad (2.22)$$

CHAPTER 3

MULTIFOCAL INTERFEROMETRIC SYNTHETIC APERTURE MICROSCOPY

Seeing the trade-off OCT is facing and the advantages and challenges of ISAM and multifocal OCT, we have developed a new imaging technique which combines the advantages of both multifocal OCT and ISAM. By applying a coherent combination of the reconstruction of each channel with appropriate regularization, higher lateral resolution and signal-to-noise ratio can be achieved without artifacts from the synthesis of the data sets. The experiment is similar to conventional OCT, except multiple channels, each with a different focus, are used.

3.1 Forward Model

The sample is described by a susceptibility $|\eta\rangle$, and the data set by $|S\rangle$. The position of the n^{th} focal plane is denoted z_{0n}. The datum at transverse-scanning position $\mathbf{r}_\parallel$, wavenumber k_0, and focal plane z_{0n} is denoted $\left\langle \mathbf{r}_\parallel, k_0, z_{0n} | S \right\rangle$. Transverse wavevector states are denoted $\left|\mathbf{k}_\parallel\right\rangle$ so that $\left\langle \mathbf{r}_\parallel | \mathbf{k}_\parallel \right\rangle = \frac{1}{2\pi} e^{-i\mathbf{k}_\parallel \cdot \mathbf{r}_\parallel}$.

Equation (19.26) in [26] provides a good starting point to this problem. The contribution to the signal from each aperture at transverse-scanning position $\mathbf{r}_a$ to the detection aperture at $\mathbf{r}_b$ can be expressed as

$$\begin{aligned} \langle \mathbf{r}_a, \mathbf{r}_b, k | S \rangle &= \int \mathrm{d}^2\mathbf{k}''_\parallel \int \mathrm{d}^2\mathbf{k}'_\parallel \int \mathrm{d}^2\mathbf{r}_\parallel \mathrm{d}z e^{i\mathbf{k}''_\parallel \cdot \mathbf{r}_b} \tilde{g}_b(\mathbf{k}''_\parallel, \mathbf{k}) \left\langle \mathbf{k}''_\parallel | \mathbf{G}_{z_b} | \mathbf{r} \right\rangle \\ &\quad \times \left\langle \mathbf{r}_\parallel | \mathbf{K}_{z_a - z} | \mathbf{k}'_\parallel \right\rangle e^{-i\mathbf{k}'_\parallel \cdot \mathbf{r}_a} \tilde{g}_a(\mathbf{k}'_\parallel, k) \left\langle k | U_0 \right\rangle \left\langle \mathbf{r} | \eta \right\rangle . \end{aligned} \tag{3.1}$$

The signal S_n detected from aperture n can be expressed as the sum of the contributions from each illumination aperture m, denoted as S_{mn}, as is illustrated in Figure 3.1. Here we assume the transverse-scanning position of

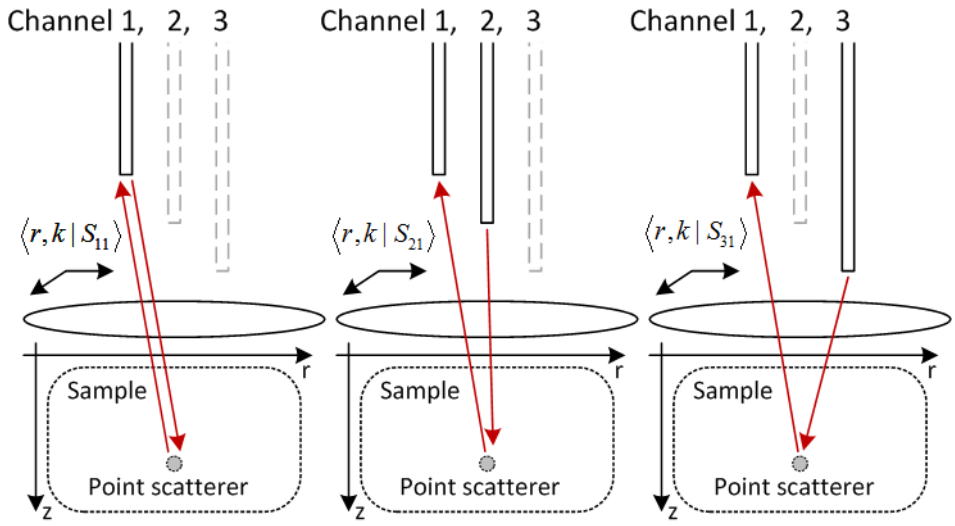

Figure 3.1: Illustration of the different components of the detected signal in multifocal OCT.

the illumination aperture is infinitely close to that of the detection aperture. Therefore, we can set $\mathbf{r}_a = \mathbf{r}_b = \mathbf{r}_0$, $g_a = g_b = g$, so that the problem is converted to single static case with illumination focal plane at depth of z_{0m} and detection focal plane at z_{0n},

$$\begin{aligned}
\langle \mathbf{r}_0, k|S_n\rangle \quad &= \sum_m \langle \mathbf{r}_0, k|S_{mn}\rangle \\
&= \int \mathrm{d}^2\mathbf{k}''_{\parallel} \int \mathrm{d}^2\mathbf{k}'_{\parallel} \int \mathrm{d}^2\mathbf{r}_{\parallel}\, \mathrm{d}z\, e^{i(\mathbf{k}''_{\parallel}-\mathbf{k}'_{\parallel})\cdot r_0} \tilde{g}(k'',k) \\
&\times [ie^{-i\mathbf{k}''_{\parallel}\cdot\mathbf{r}_{\parallel}} \frac{e^{i\sqrt{k_0^2-\mathbf{k}''^2_{\parallel}}(z_{0n}-z)}}{\sqrt{k_0^2-\mathbf{k}''^2_{\parallel}}}][\tfrac{1}{2\pi} e^{i\mathbf{r}_{\parallel}\cdot k'_{\parallel}} e^{i\sqrt{k_0^2-\mathbf{k}_{\parallel}'^2}} \sum_m e^{(z_{0m}-z)}] \\
&\times \tilde{g}(\mathbf{k}'_{\parallel},k)\, \langle k|U_0\rangle\, \langle \mathbf{r}|\eta\rangle\, . \qquad (3.2)
\end{aligned}$$

By performing a change of basis of the equation above, the multi-foci version of Equation 19.29 in [26] can be derived, as is shown in Equations

3.3 and 3.4 below:

$$\begin{aligned}\left\langle \mathbf{k}_{\parallel}, k|S_n\right\rangle &= \sum_m \left\langle \mathbf{k}_{\parallel}, k|S_{mn}\right\rangle \\ &= \sum_m \int \mathrm{d}^2\mathbf{r}_0 \left\langle \mathbf{k}_{\parallel}, k|\mathbf{r}_0, k\right\rangle \left\langle \mathbf{r}_0, k|S_{mn}\right\rangle \\ &= \sum_m \langle k|U_0\rangle \int \mathrm{d}z\ \tilde{h}(\mathbf{k}_{\parallel}, z, k, z_{0n}, z_{0m})[\left\langle \mathbf{k}_{\parallel}\right| \langle z|\eta\rangle], \quad (3.3)\end{aligned}$$

where

$$\begin{aligned}\tilde{h}(\mathbf{k}_{\parallel}, z, k, z_{0n}, z_{0m}) = \int \mathrm{d}^2\mathbf{k}''_{\parallel}\ \frac{\tilde{g}(\mathbf{k}'', k)\tilde{g}(\mathbf{k}''_{\parallel} - \mathbf{k}_{\parallel}, k)}{\sqrt{k_0^2 - \mathbf{k}''^2_{\parallel}}} \\ \times \sum_m e^{i\sqrt{k_0^2-\mathbf{k}''^2_{\parallel}}(z_{0n}-z)+i\sqrt{k_0^2-(\mathbf{k}''_{\parallel}-\mathbf{k}_{\parallel})^2}(z_{0m}-z)}. \quad (3.4)\end{aligned}$$

The function $\tilde{h}(\mathbf{k}_{\parallel}, z, k)$ in Equation 3.4 describes the point spread function of the multifocal OCT forward problem, which consists of several components located at different depths. Equation 3.3 can be understood as a mix of filtering of the sample susceptibility in k_x and k_y axes in the frequency domain and a convolution along the z-axis in the spatial domain, which corresponds to the convolution of point-spread function in 3D spatial domain.

In order to eliminate the stacked point spread function, which is computationally too expensive to deconvolve, we assume that the path-length difference between channels is much larger than the source coherence length so that cross-talk S_{mn} where $m \neq n$ may be neglected. This can be achieved experimentally by inserting different length of fiber before each aperture. With this assumption, the signal detected from the n^{th} aperture only consists of the back-scattering caused by the illumination from itself, resulting an simplified point spread function, as is described by

$$\left\langle \mathbf{k}_{\parallel}, k|S_n\right\rangle = \left\langle \mathbf{k}_{\parallel}, k|S_{nn}\right\rangle = \langle k|U_0\rangle \int \mathrm{d}z\ \tilde{h}'(\mathbf{k}_{\parallel}, z, k)[\left\langle \mathbf{k}_{\parallel}\right| \langle z|\eta\rangle], \quad (3.5)$$

where

$$\tilde{h}'(\mathbf{k}_{\parallel}, z, k) = \int \mathrm{d}^2\mathbf{k}''_{\parallel} \frac{\tilde{g}(\mathbf{k}''_{\parallel}, k)\tilde{g}(\mathbf{k}''_{\parallel} - \mathbf{k}_{\parallel}, k)}{\sqrt{k_0^2 - \mathbf{k}''^2_{\parallel}}} e^{i\left[\sqrt{k_0^2-\mathbf{k}''^2_{\parallel}}+\sqrt{k_0^2-(\mathbf{k}''_{\parallel}-\mathbf{k}_{\parallel})^2}\right](z_{0n}-z)}. \quad (3.6)$$

Since we have multiple sets of signals with different focal plane depths, we add the dimension of z_{0n} to accommodate all datasets obtained from each focal plane z_{0n}. Thus, $|\eta\rangle$ becomes a vector in $L_2(\mathbb{R}^4)$. The method of stationary phase can be applied when $|z_{0n} - z|$ is large compared to wavelength, where the phase is stationary around $\mathbf{k}_{\parallel}^{\prime\prime(stat.)} = \frac{\mathbf{k}_{\parallel}}{2}$ [26], resulting in an simplified asymptotics result,

$$\left\langle \mathbf{k}_{\parallel}, k, z_{0n}|S\right\rangle = H_F(\mathbf{k}_{\parallel}, z_{0n}) \left\langle \mathbf{k}_{\parallel}, z_{0n}\right| \int \mathrm{d}z \left\langle -2\sqrt{k_0^2 - (\mathbf{k}_{\parallel}/2)^2}|z\right\rangle \times |z - z_{0n}|^{-1} \left\langle z|\eta\right\rangle . \quad (3.7)$$

When $|z_{0n} - z|$ is small compared to wavelength, the asymptotic result is

$$\left\langle \mathbf{k}_{\parallel}, k, z_{0n}|S\right\rangle = H_F(\mathbf{k}_{\parallel}, z_{0n}) \left\langle \mathbf{k}_{\parallel}, z_{0n}\right| \int \mathrm{d}z \left\langle -2\sqrt{k_0^2 - (\mathbf{k}_{\parallel}/2)^2}|z\right\rangle \times 1^{-1} \left\langle z|\eta\right\rangle . \quad (3.8)$$

The term $|z - z_{0n}|^{-1}$ and 1^{-1} in Equation 3.7 and 3.8 can be replaced with $w_0/w(z)$, which is 1^{-1} when $|z_{0n} - z|$ is small and decays with $|z - z_{0n}|^{-1}$ when $|z_{0n} - z|$ is large. In this way both asymptotic results can be generalized by

$$\left\langle \mathbf{k}_{\parallel}, k, z_{0n}|S\right\rangle = H_F(\mathbf{k}_{\parallel}, z_{0n}) \left\langle \mathbf{k}_{\parallel}, z_{0n}\right| \int \mathrm{d}z \left\langle -2\sqrt{k_0^2 - (\mathbf{k}_{\parallel}/2)^2}|z\right\rangle \times w_r(z, z_{0n})^{-1} \left\langle z|\eta\right\rangle , \quad (3.9)$$

where

$$H_F(\mathbf{k}_{\parallel}, z_{0n}) = \langle k|U_0\rangle \, \tilde{g}^2(\mathbf{k}_{\parallel}/2, k) e^{-2iz_{0n}\sqrt{k_0^2 - (\mathbf{k}_{\parallel}/2)^2}}, \quad (3.10)$$

and $w_r(z, z_{0n})$ is the relative beam width compared to w_0,

$$w_r(z, z_{0n}) = \frac{w(z, z_{0n})}{w_0} = \frac{1}{w_0}\sqrt{w_0^2 + \left[\frac{\lambda(z - z_0)}{\pi w_0}\right]^2} = \sqrt{1 + \left[\frac{\lambda(z - z_0)}{\pi w_0^2}\right]^2}. \quad (3.11)$$

3.2 Regularized Inverse

At this stage we have formed a complete forward model of multifocal ISAM, which relates the susceptibility distribution $|\eta\rangle$ of the sample to the signal $|\eta\rangle$ detected from the aperture. The next step is to derive its inverse based on the forward problem, which enables us to reconstruct the susceptibility distribution from the detected signal. We start from Equation 3.12 below, which is equivalent to Equation 3.9:

$$\begin{aligned} |S\rangle &= \int \mathrm{d}^2\mathbf{k}_\parallel \, \mathrm{d}k_0 \, \mathrm{d}z_{0n} \left|\mathbf{k}_\parallel, k_0, z_{0n}\right\rangle H_F(\mathbf{k}_\parallel, z_{0n}) \left\langle \mathbf{k}_\parallel, z_{0n}\right| \\ &\quad \times \int \mathrm{d}z \, \mathrm{d}z'_{0n} \left\langle -2\sqrt{k_0^2 - (\mathbf{k}_\parallel/2)^2}|z, z'_{0n}\right\rangle w_r(z, z'_{0n})^{-1} \langle z|\eta\rangle \end{aligned} \tag{3.12}$$

The detected signal $|S\rangle$ can be seen as the result of two operators P and Z acting on the sample susceptibility $|\eta\rangle$, so that $|S\rangle = PZ\,|\eta\rangle$. As is described by Equation 3.14 and 3.13, the P operator takes the data from $|\eta\rangle$ and remaps on to a different grid,

$$\begin{aligned} P = \int \mathrm{d}^2\mathbf{k}_\parallel \, \mathrm{d}k_0 \, \mathrm{d}z_{0n} \left|\mathbf{k}_\parallel, k_0, z_{0n}\right\rangle H_F(\mathbf{k}_\parallel, z_{0n}) \\ \times \left\langle \mathbf{k}_\parallel, -2\sqrt{k_0^2 - (\mathbf{k}_\parallel/2)^2}, z_{0n}\right| . \end{aligned} \tag{3.13}$$

The Z operator takes data from $|\eta\rangle$ and applies a depth dependent attenuation of $|z - z_{0n}|^{-1}$ in magnitude in the z dimension,

$$Z = \int \mathrm{d}z \, \mathrm{d}z'_{0n} \, |z, z'_{0n}\rangle \, w_r(z, z'_{0n})^{-1} \, \langle z| \, . \tag{3.14}$$

This can be imagined as the result of the local intensity of the illuminating beam attenuates as it spreads in the transverse direction.

To reconstruct $|\eta\rangle$, we need to derive the pseudoinverse of the two operators P and Z respectively. Here we denote them as P^+ and Z^+. The reconstructed $|\eta\rangle$ then can be expressed as

$$|\eta\rangle = Z^+ P^+ \, |S\rangle \, . \tag{3.15}$$

The pseudoinverse of P can be derived in the following steps using $P^+ =$

$(P^*P)^{-1}P^*$,

$$P^*P = \int \mathrm{d}^2\mathbf{k}_\parallel \, \mathrm{d}k_0 \, \mathrm{d}z_{0n} \left| \mathbf{k}_\parallel, z_{0n}, -2\sqrt{k_0^2 - (\mathbf{k}_\parallel/2)^2} \right\rangle \times |H_F(\mathbf{k}_\parallel, z_{0n})|^2 \left\langle \mathbf{k}_\parallel, z_{0n}, -2\sqrt{k_0^2 - (\mathbf{k}_\parallel/2)^2} \right| . \tag{3.16}$$

For simplicity, a change of variables is performed. Let

$$\beta = -2\sqrt{k_0^2 - (\mathbf{k}_\parallel/2)^2}, \tag{3.17}$$

so that

$$P^*P = \int \mathrm{d}^2\mathbf{k}_\parallel \, \mathrm{d}\beta \, \mathrm{d}z_{0n} \left| \mathbf{k}_\parallel, z_{0n}, \beta \right\rangle \frac{\beta |H_F(\mathbf{k}_\parallel, z_{0n})|^2}{2\sqrt{\beta^2 + \mathbf{k}_\parallel^{\,2}}} \left\langle \mathbf{k}_\parallel, z_{0n}, \beta \right| . \tag{3.18}$$

The singular value in the above equation can be identified as

$$\sigma^2 = \frac{\beta |H_F(\mathbf{k}_\parallel, z_{0n})|^2}{2\sqrt{\beta^2 + \mathbf{k}_\parallel^{\,2}}}. \tag{3.19}$$

Thus, the normal operator takes the form of

$$(P^*P)^{-1} = \int \mathrm{d}^2\mathbf{k}_\parallel \, \mathrm{d}\beta \, \mathrm{d}z_{0n} \left| \mathbf{k}_\parallel, z_{0n}, \beta \right\rangle \frac{2\sqrt{\beta^2 + \mathbf{k}_\parallel^{\,2}}}{\beta |H_F(\mathbf{k}_\parallel, z_{0n})|^2} \left\langle \mathbf{k}_\parallel, z_{0n}, \beta \right| . \tag{3.20}$$

The pseudoinverse of operator P can then be expressed as

$$\begin{aligned} P^+ &= (P^*P)^{-1}P^* \\ &= \int \mathrm{d}^2\mathbf{k}_\parallel \, \mathrm{d}\beta \, \mathrm{d}z_{0n} \left| \mathbf{k}_\parallel, z_{0n}, \beta \right\rangle H_F^{-1}(\mathbf{k}_\parallel, z_{0n}) \\ &\quad \times \left\langle \mathbf{k}_\parallel, z_{0n}, \frac{1}{2}\sqrt{\beta^2 + \mathbf{k}_\parallel^{\,2}} \right| . \end{aligned} \tag{3.21}$$

Using similar method, the exact inverse of operator Z can also be derived, that is

$$Z^{-1} = \int \mathrm{d}z \, \mathrm{d}z_{0n} \left| z \right\rangle w_r(z, z_{0n}) \left\langle z, z_{0n} \right| . \tag{3.22}$$

For different noise model, corresponding regularization can be applied by

replacing $w_r(z, z_{0n})$ with its function, so that

$$Z^+ = \int \mathrm{d}z \; \mathrm{d}z_{0n} \, |z\rangle \, R\left[w_r(z, z_{0n})\right] \langle z, z_{0n}| \,, \tag{3.23}$$

to achieve minimum L_2 error solution.

Here for the multiplicative noise, Tikhonov regularization promises the minimum L_2 error solution of the problem. The regularizer of Tikhonov regularization is

$$R\left(w_r(z, z_{0n}\right) = \frac{w_r(z, z_{0n})^{-1}}{w_r(z, z_{0n})^{-2} + \lambda}. \tag{3.24}$$

Thus, the regularized inverse of the Z operator is

$$Z^+ \;\; = \;\; \int \mathrm{d}z \; \mathrm{d}z_{0n} \, |z\rangle \, \frac{w_r(z, z_{0n})}{1 + \lambda w_r(z, z_{0n})^2} \, \langle z, z_{0n}| \,. \tag{3.25}$$

The Tikhonov regularized solution of the inverse problem is then

$$\begin{aligned} \langle r|\eta\rangle \;\; = \;\; & \int dz_{0n} \frac{w_r(z, z_{0n})}{1 + \lambda w_r(z, z_{0n})^2} \int \mathrm{d}^2\mathbf{k}_\parallel \left\langle \mathbf{r}_\parallel | \mathbf{k}_\parallel \right\rangle \int d\beta \, \langle z| - \beta\rangle \\ & \times H_F^{-1}(\mathbf{k}_\parallel, z_{0n}) \left\langle \mathbf{k}_\parallel, \frac{1}{2}\sqrt{\beta^2 + \mathbf{k}_\parallel{}^2}, z_{0n}|S \right\rangle, \end{aligned} \tag{3.26}$$

where the factor H_F^{-1} depends on $\mathbf{k}_\parallel$, β, and the focal position z_{0n} [36]. In reality, we can only have discrete number of apertures, the discretized version can be expressed as

$$\begin{aligned} \langle r|\eta\rangle \;\; = \;\; & \sum_{n=1}^{N} \frac{w_r(z, z_{0n})}{1 + \lambda w_r(z, z_{0n})^2} \int \mathrm{d}^2\mathbf{k}_\parallel \left\langle \mathbf{r}_\parallel | \mathbf{k}_\parallel \right\rangle \int d\beta \, \langle z| - \beta\rangle \\ & \times H_F^{-1}(\mathbf{k}_\parallel, z_{0n}) \left\langle \mathbf{k}_\parallel, \frac{1}{2}\sqrt{\beta^2 + \mathbf{k}_\parallel{}^2}, z_{0n}|S \right\rangle, \end{aligned} \tag{3.27}$$

where instead of performing an integration on z_{0n}, we take the sum over all z_{0n}.

3.3 Simulation

A computer simulation demonstrates the regularized solution of the multifocal ISAM inverse problem in Figure 3.2. The sample used in the simulation consists of a series of point-scatterers on the x-z plane with 5μm separation in depth between neighboring point-scatterers, as in the simulation in Figure 1.7. An OCT system with an NA of 0.75, refractive index of 1, and wavelength of 900nm to 1000nm was used, resulting in a transverse resolution of 0.6μm and a Rayleigh range of 1.25μm in air.

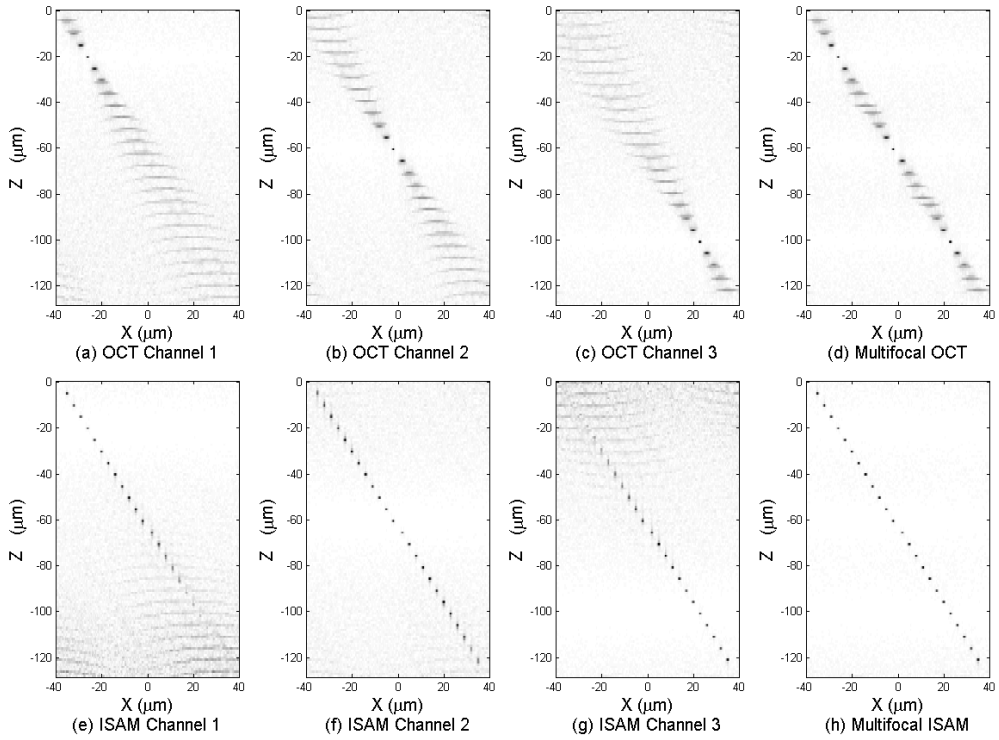

Figure 3.2: Panels a), b), and c) are three channels of OCT data, each focused at -20μm, -60μm, and -100μm respectively. Panel d) is the multifocal OCT reconstruction based on a), b), and c). Panel e), f), and g) are three channels of ISAM reconstruction based on a), b), and c) respectively. Panel h) is the multifocal ISAM reconstruction based on e), f), and g).

The results in Figure 3.2 a)-c) show how the spreading in the OCT image acquired with focal plane at different depth becomes more severe at large distances from focus. Figure 3.2 d) shows the stitched image multibeam OCT synthetized from data in a)-c). Although d) sees an immediate improvement over a)-c), the transverse resolution achieved by multibeam OCT still varies

spatially.

The results in Figure 3.2 e)-g) demonstrate how the regularization works as weightings to scale-down the noisy signal far from focus at each channel. The results in Figure 3.2 h) show the regularized inverse solution works effectively in correcting the defocus and coherently combining the three datasets to achieve a reconstruction with spatially invariant resolution. Compared with the multibeam OCT image at d), resolution in h) again shows a significant improvement.

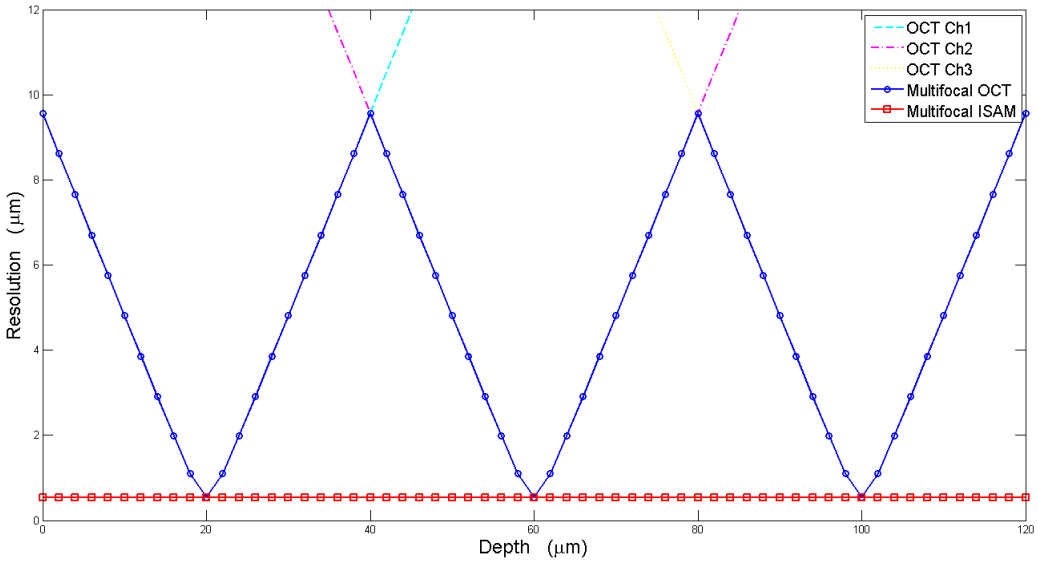

Figure 3.3: Theoretical transverse resolution for three channels of OCT, multifocal OCT and multifocal ISAM, based on a three-aperture multifocal OCT system with focal plane at -20μm, -60μm, and -100μm.

With the same parameters as above, Figures 3.3 and 3.4 show plots of theoretical transverse resolution and simulation measurement of multibeam OCT and multifocal ISAM. Multifocal ISAM shows superior transverse resolution, especially at larger distance from each focus, compared to multibeam OCT.

Figure 3.4 shows a plot of theoretical signal-to-noise ratio of single-focal ISAM and multifocal ISAM. Multifocal ISAM shows superior SNR characteristics at all depths, compared to single-focal ISAM.

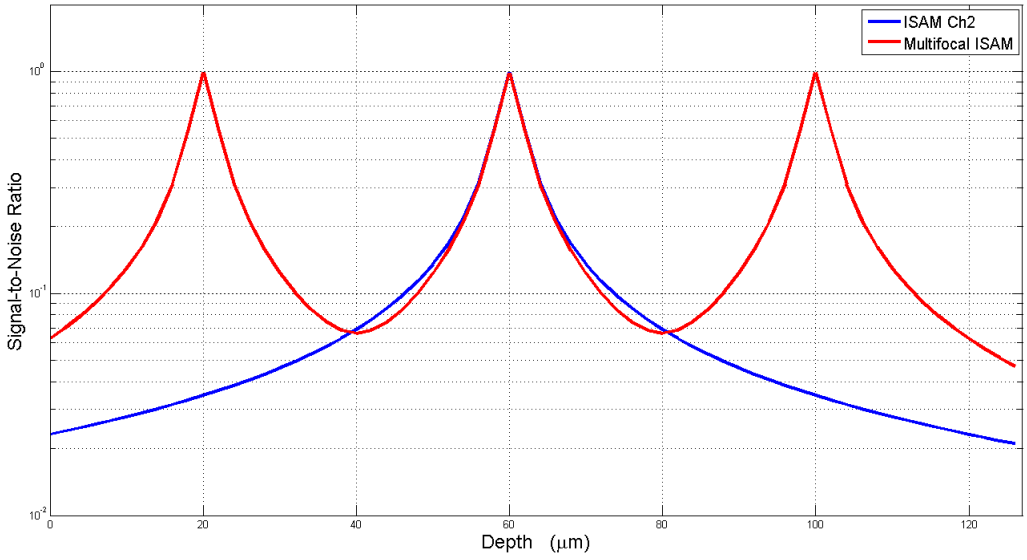

Figure 3.4: Theoretical SNR of single-focal ISAM and multifocal ISAM, based on a three-aperture multifocal OCT system with focal plane at -20μm, -60μm, and -100μm.

3.4 Experimental Results

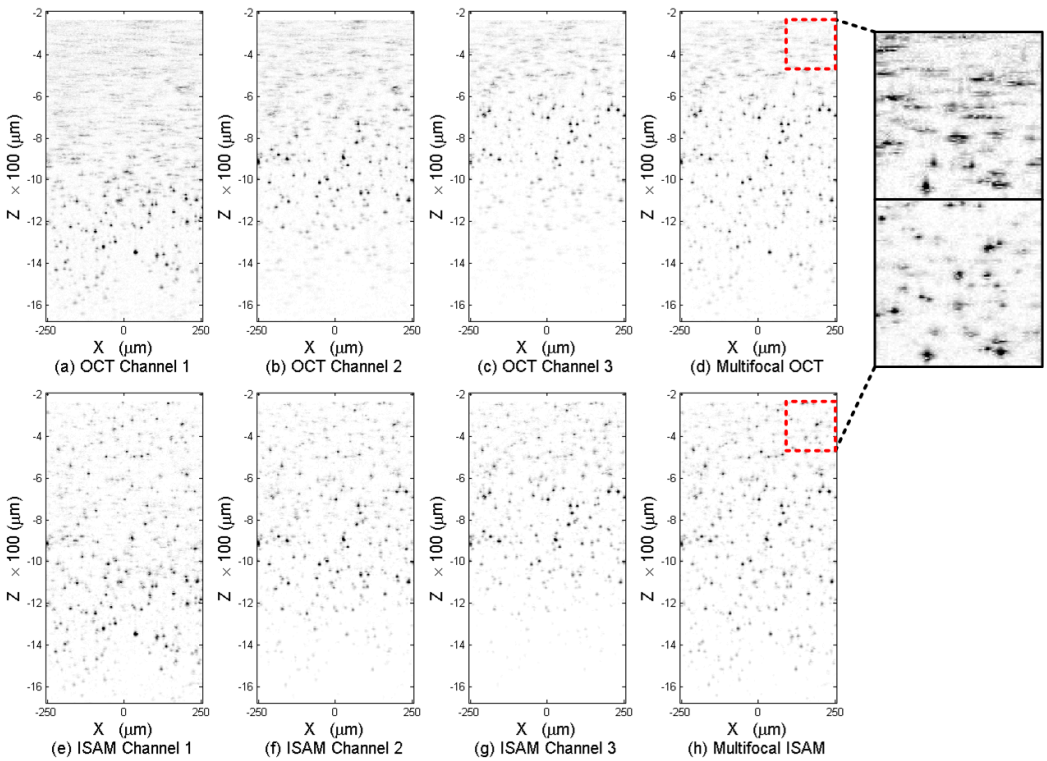

Figure 3.5: Panels a), b), and c) are three channels of OCT data, each focused at -1200μm, -1000μm, and -800μm respectively. Panel d) is the multifocal OCT reconstruction based on a), b), and c). Panels e), f), and g) are three channels of ISAM reconstruction based on a), b), and c) respectively. Panel h) is the multifocal ISAM reconstruction based on e), f), and g).

Experimental data have been taken and the regularized inverse solution for multifocal ISAM has been applied to demonstrate the multifocal ISAM reconstruction. Three datasets were acquired separately using a single channel SD-OCT setup. The focal plane depths of the scanning beams were adjusted before each scan. As shown in Figure 3.5, three datasets a), b), and c) were acquired with focal plane at -1200μm, -1000μm, and -800μm respectively. The OCT system has a NA of 0.1, and the optical spectrum recorded by the spectrometer had central wavelength of 1330nm and FWHM bandwidth of 150nm. Thus, the setup has a transverse resolution of $\sim 7\mu$m and a Rayleigh range of $\sim 100\mu$m in air. The sample consists of a collection of sub-resolution sized TiO_2 particles embedded in a semitransparent silicone matrix, which

has a refractive index of 1.4.

Figure 3.5 a), b) and c) are the OCT reconstructions of each set of signals. It can be observed that the reconstructions become defocused far away from their focal plane; thus, each set provides $\sim 200\mu$m usable imaging depth. After applying the image stitching method over a), b), and c), Figure 3.5 d) is the multifocal OCT reconstruction of the datasets. It provides an imaging depth of $\sim 600\mu$m, from -600μm to -1400μm.

By comparing Figure 3.5 d) with h), it can be observed that after regularized combination, the reconstruction in h) shows not only higher resolution especially at far form focus, but also high SNR throughout all depths [36].

3.5 Cost Analysis and Range of Application

Although both our simulation and experimental demonstration involve three foci, the technique can be readily extended to accommodate arbitrary numbers of foci.

Data for multifocal ISAM can be acquired either in parallel using multifocal OCT setup or in series using conventional OCT setup. For serial acquisition, simply repeat OCT scan multiple times, with the depth of focal plane at each time forming the desired arithmetic sequence. Serial acquisition trades longer acquisition time (proportional to number of foci desired) for lower setup complexity.

The computational cost for multifocal ISAM is proportional to the number of foci desired. Reconstruction at a similar scale to Figure 3.5 can be easily performed using current mainstream desktop computer within minutes. Furthermore, it is possible to implement the algorithm on a GPU using parallel programming language, such as CUDA, to achieve real time reconstruction [37, 38].

Multifocal ISAM is based on the assumption of first Born approximation, as in OCT. Under such approximation, single scattering is assumed and higher order scattering is omitted. In many applications of OCT, this proves to be a good enough approximation when dealing with many kinds of samples. So, for any sample OCT can work with, multifocal ISAM can be applied to produce images with high resolution, large imaging depth, and high SNR.

CHAPTER 4

SUMMARY

We have shown that multifocal ISAM can realize the benefits of both single-focus ISAM and multibeam OCT by producing a reconstruction with uniform resolution and good signal to noise over a large range. Multifocal ISAM provides a physically meaningful method to combine multiple ISAM data from the same sample with different foci to achieve high SNR over large depth. Multifocal ISAM provides a physically meaningful method to combine multiple ISAM data from the same sample with different foci to scale up the effective imaging depth of the image.

REFERENCES

[1] D. Huang, E. A. Swanson, C. P. Lin, J. S. Schuman, W. G. Stinson, W. Chang, M. R. Hee, T. Flotte, K. Gregory, C. A. Puliafito, and J. G. Fujimoto, "Optical coherence tomography," *Science*, vol. 254, no. 5035, pp. 1178–1181, 1991.

[2] S. A. Boppart, B. E. Bouma, C. Pitris, G. J. Tearney, J. G. Fujimoto, and M. E. Brezinski, "Forward-imaging instruments for optical coherence tomography," *Optics Letters*, vol. 22, no. 21, pp. 1618–1620, 1997.

[3] S. A. Boppart, B. E. Bouma, C. Pitris, J. F. Southern, M. E. Brezinski, and J. G. Fujimoto, "In vivo cellular optical coherence tomography imaging," *Nature Medicine*, vol. 4, no. 7, pp. 861–865, 1998.

[4] J. G. Fujimoto, C. Pitris, S. A. Boppart, and M. E. Brezinski, "Optical coherence tomography: An emerging technology for biomedical imaging and optical biopsy," *Neoplasia*, vol. 2, no. 1-2, pp. 9–25, 2000.

[5] S. A. Boppart, W. Luo, D. L. Marks, and K. W. Singletary, "Optical coherence tomography: feasibility for basic research and image-guided surgery of breast cancer," *Breast Cancer Research and Treatment*, vol. 84, no. 2, pp. 85–97, 2004.

[6] Z. Yaqoob, J. G. Wu, E. J. McDowell, X. Heng, and C. H. Yang, "Methods and application areas of endoscopic optical coherence tomography," *Journal of Biomedical Optics*, vol. 11, no. 6, 2006.

[7] M. Wojtkowski, A. Kowalczyk, R. Leitgeb, and A. F. Fercher, "Full range complex spectral optical coherence tomography technique in eye imaging," *Optics Letters*, vol. 27, no. 16, pp. 1415–1417, 2002.

[8] E. A. Swanson, J. A. Izatt, M. R. Hee, D. Huang, C. P. Lin, J. S. Schuman, C. A. Puliafito, and J. G. Fujimoto, "In vivo retinal imaging by optical coherence tomography," *Optics Letters*, vol. 18, no. 21, pp. 1864–1866, 1993.

[9] J. A. Izatt, M. R. Hee, E. A. Swanson, C. P. Lin, D. Huang, J. S. Schuman, C. A. Puliafito, and J. G. Fujimoto, "Micrometer-scale resolution imaging of the anterior eye in-vivo with optical coherence tomography," *Archives of Ophthalmology*, vol. 112, no. 12, pp. 1584–1589, 1994.

[10] J. S. Schuman, M. R. Hee, C. A. Puliafito, C. Wong, T. Pedutkloizman, C. P. Lin, E. Hertzmark, J. A. Izatt, E. A. Swanson, and J. G. Fujimoto, "Quantification of nerve fiber layer thickness in normal and glaucomatous eyes using optical coherence tomography," *Archives of Ophthalmology*, vol. 113, no. 5, pp. 586–596, 1995.

[11] J. R. Wilkins, C. A. Puliafito, M. R. Hee, J. S. Duker, E. Reichel, J. G. Coker, J. S. Schuman, E. A. Swanson, and J. G. Fujimoto, "Characterization of epiretinal membranes using optical coherence tomography," *Ophthalmology*, vol. 103, no. 12, pp. 2142–2151, 1996.

[12] V. Guedes, J. S. Schuman, E. Hertzmark, G. Wollstein, A. Correnti, R. Mancini, D. Lederer, S. Voskanian, L. Velazquez, H. M. Pakter, T. Pedut-Kloizman, J. G. Fujimoto, and C. Mattox, "Optical coherence tomography measurement of macular and nerve fiber layer thickness in normal and glaucomatous human eyes," *Ophthalmology*, vol. 110, no. 1, pp. 177–189, 2003.

[13] M. Wojtkowski, V. Srinivasan, J. G. Fujimoto, T. Ko, J. S. Schuman, A. Kowalczyk, and J. S. Duker, "Three-dimensional retinal imaging with high-speed ultrahigh-resolution optical coherence tomography," *Ophthalmology*, vol. 112, no. 10, pp. 1734–1746, 2005.

[14] J. Welzel, "Optical coherence tomography in dermatology: a review," *Skin Research and Technology*, vol. 7, no. 1, pp. 1–9, 2001.

[15] M. C. Pierce, J. Strasswimmer, B. H. Park, B. Cense, and J. F. de Boer, "Advances in optical coherence tomography imaging for dermatology," *Journal of Investigative Dermatology*, vol. 123, no. 3, pp. 458–463, 2004.

[16] T. Gambichler, G. Moussa, M. Sand, D. Sand, P. Altmeyer, and K. Hoffmann, "Applications of optical coherence tomography in dermatology," *Journal of Dermatological Science*, vol. 40, no. 2, pp. 85–94, 2005.

[17] S. A. Boppart, G. J. Tearney, B. E. Bouma, J. F. Southern, M. E. Brezinski, and J. G. Fujimoto, "Noninvasive assessment of the developing xenopus cardiovascular system using optical coherence tomography," *Proceedings of the National Academy of Sciences of the United States of America*, vol. 94, no. 9, pp. 4256–4261, 1997.

[18] S. Zhong, Y.-C. Shen, L. Ho, R. K. May, J. A. Zeitler, M. Evans, P. F. Taday, M. Pepper, T. Rades, K. C. Gordon, R. Mller, and P. Kleinebudde, "Non-destructive quantification of pharmaceutical tablet coatings using terahertz pulsed imaging and optical coherence tomography," *Optics and Lasers in Engineering*, vol. 49, no. 3, pp. 361–365, Mar. 2011. [Online]. Available: http://linkinghub.elsevier.com/retrieve/pii/S0143816610002472

[19] P. Liu, R. M. Groves, and R. Benedictus, "Quality assessment of aerospace materials with optical coherence tomography," C. Gorecki, A. K. Asundi, and W. Osten, Eds., Apr. 2012. [Online]. Available: http://proceedings.spiedigitallibrary.org/proceeding.aspx?articleid=1316152 pp. 84 300I–84 300I–7.

[20] R. Leitgeb, C. K. Hitzenberger, and A. F. Fercher, "Performance of fourier domain vs. time domain optical coherence tomography," *Optics Express*, vol. 11, no. 8, pp. 889–894, 2003.

[21] J. F. de Boer, B. Cense, B. H. Park, M. C. Pierce, G. J. Tearney, and B. E. Bouma, "Improved signal-to-noise ratio in spectral-domain compared with time-domain optical coherence tomography," *Optics Letters*, vol. 28, no. 21, pp. 2067–2069, 2003.

[22] R. A. Leitgeb, M. Villiger, A. H. Bachmann, L. Steinmann, and T. Lasser, "Extended focus depth for fourier domain optical coherence microscopy," *Optics Letters*, vol. 31, no. 16, pp. 2450–2452, 2006.

[23] M. A. Choma, M. V. Sarunic, C. H. Yang, and J. A. Izatt, "Sensitivity advantage of swept source and fourier domain optical coherence tomography," *Optics Express*, vol. 11, no. 18, pp. 2183–2189, 2003.

[24] A. Dubois, L. Vabre, A.-C. Boccara, and E. Beaurepaire, "High-resolution full-field optical coherence tomography with a linnik microscope," *Applied Optics*, vol. 41, no. 4, p. 805, Feb. 2002. [Online]. Available: http://www.opticsinfobase.org/abstract.cfm?URI=ao-41-4-805

[25] G. J. Tearney, S. A. Boppart, B. E. Bouma, M. E. Brezinski, N. J. Weissman, J. F. Southern, and J. G. Fujimoto, "Scanning single-mode fiber optic catheter-endoscope for optical coherence tomography," *Optics Letters*, vol. 21, no. 7, p. 543, Apr. 1996. [Online]. Available: http://www.opticsinfobase.org/abstract.cfm?URI=ol-21-7-543

[26] P. S. Carney, S. G. Adie, and S. A. Boppart, "Interferometric synthetic aperture microscopy," *Emerging Imaging Technologies in Medicine*, p. 293, 2012.

[27] R. K. K. Wang, "Signal degradation by coherence tomography multiple scattering in optical of dense tissue: a monte carlo study towards optical clearing of biotissues," *Physics in Medicine and Biology*, vol. 47, no. 13, pp. 2281–2299, 2002.

[28] B. Karamata, M. Laubscher, M. Leutenegger, S. Bourquin, T. Lasser, and P. Lambelet, "Multiple scattering in optical coherence tomography. i. investigation and modeling," *Journal of the Optical Society of America a-Optics Image Science and Vision*, vol. 22, no. 7, pp. 1369–1379, 2005.

[29] J. Holmes, S. Hattersley, N. Stone, F. Bazant-Hegemark, and H. Barr, "Multi-channel fourier domain OCT system with superior lateral resolution for biomedical applications," vol. 6847, 2008. [Online]. Available: http://dx.doi.org/10.1117/12.761655 pp. 68 470O–68 470O–9.

[30] J. Holmes, "Theory and applications of multi-beam OCT," vol. 7139, 2008. [Online]. Available: http://dx.doi.org/10.1117/12.821006 pp. 713 908–713 908–7.

[31] J. Holmes and S. Hattersley, "Image blending and speckle noise reduction in multi-beam OCT," vol. 7168, 2009. [Online]. Available: http://dx.doi.org/10.1117/12.808575 pp. 71 681N–71 681N–8.

[32] T. S. Ralston, D. L. Marks, P. S. Carney, and S. A. Boppart, "Interferometric synthetic aperture microscopy," *Nature Physics*, vol. 3, no. 2, pp. 129–134, 2007.

[33] B. J. Davis, S. C. Schlachter, D. L. Marks, T. S. Ralston, S. A. Boppart, and P. S. Carney, "Nonparaxial vector-field modeling of optical coherence tomography and interferometric synthetic aperture microscopy," *Journal of the Optical Society of America a-Optics Image Science and Vision*, vol. 24, no. 9, pp. 2527–2542, 2007.

[34] B. J. Davis, D. L. Marks, T. S. Ralston, P. S. Carney, and S. A. Boppart, "Interferometric synthetic aperture microscopy: Computed imaging for scanned coherent microscopy," *Sensors*, vol. 8, no. 6, pp. 3903–3931, 2008.

[35] T. S. Ralston, S. G. Adie, D. L. Marks, S. A. Boppart, and P. S. Carney, "Cross-validation of interferometric synthetic aperture microscopy and optical coherence tomography," *Optics Letters*, vol. 35, no. 10, pp. 1683–1685, 2010.

[36] Y. Xu, X. K. B. Chng, S. G. Adie, S. A. Boppart, and P. S. Carney, "Multifocal interferometric synthetic aperture microscopy," in *Frontiers in Optics*. Optical Society of America, 2013, pp. FW1D–5.

[37] T. S. Ralston, D. L. Marks, P. S. Carney, and S. A. Boppart, "Real-time interferometric synthetic aperture microscopy," *Optics express*, vol. 16, no. 4, p. 2555, 2008.

[38] A. Ahmad, N. Shemonski, S. G. Adie, H. Kim, W.-M. W. Hwu, P. S. Carney, and S. Boppart, "High-speed interferometric synthetic aperture microscopy on a graphics processing unit," in *Frontiers in Optics*. Optical Society of America, 2012.